IOP Publishing J. Phys. Mater. 8 (2025) 015007 https://doi.org/10.1088/2515-7639/ad9e2f

Journal of Physics: Materials

OPEN ACCESS

RECEIVED
12 August 2024

REVISED
22 November 2024

ACCEPTED FOR PUBLICATION
11 December 2024

PUBLISHED
23 December 2024

PAPER

Towards high loading cesium lead halide nanocomposites for radiation detection

Jan Král[1,2,*], Kateřina Děcká[1,2], Vojtěch Zabloudil[1,3], Petr Liška[4,5], František Hájek[2,6], Michal Horák[5], Václav Čuba[1], Eva Mihóková[1,2] and Etiennette Auffray[3]

[1] Faculty of Nuclear Sciences and Physical Engineering, Czech Technical University in Prague, Břehová 7, Prague 115 19, Czech Republic
[2] Institute of Physics of the Czech Academy of Sciences, Cukrovarnická 10, Prague 162 00, Czech Republic
[3] CERN Esplanade des Particules 1, Meyrin 1211, Switzerland
[4] Institute of Physical Engineering, Faculty of Mechanical Engineering, Brno University of Technology, Technická 2896/2, 616 69 Brno, Czech Republic
[5] Central European Institute of Technology, Brno University of Technology, Purkyňova 656/123, 612 00 Brno, Czech Republic
[6] Institute of High Pressure Physics 'Unipress', Polish Academy of Sciences, Sokolowska 29/37, 01-142 Warsaw, Poland
[*] Author to whom any correspondence should be addressed.

E-mail: kralja13@fjfi.cvut.cz

Keywords: cesium lead halide nanocrystals, nanocomposite, radiation detection, fast timing

Supplementary material for this article is available online

Abstract

Cesium lead halide nanocrystals (NCs) and their nanocomposites have attracted a lot of attention in the field of radiation detection thanks to their excellent luminescent properties, especially their potential for fast timing. However, most research on their nanocomposites focuses on low loadings (around 1 wt%) which is insufficient for detecting high-energy X-rays or γ-rays. There have been only few reports exploring materials with higher loadings but all with limited success in terms of transparency of the final material. In our work, we present nanocomposites of cesium lead halide NCs with loading up to 40 wt%. We employ innovative surface functionalization of the NCs to enhance their dispersion within the matrix, thereby improving the final material transparency. We display the NC dispersion within the matrix using confocal photoluminescence microscopy and we then characterise the radioluminescent properties of nanocomposites of cesium lead bromide (CPB) and cesium lead bromochloride NCs with varying chloride content. To asses their performance as radiation detectors, we measure their timing capabilities under X-rays. Our findings reveal a significant improvement in time resolution under X-rays from previously published 300 ps for CPB polymer nanocomposites to 215 ps. When combined with increased stopping power of high NC content, this advancement holds great promise for practical applications, e.g. in time-of-flight positron emission tomography and computed tomography or high energy physics.

1. Introduction

Cesium lead halide perovskite nanocrystals (NCs) have received significant attention in recent years due to their distinctive luminescent properties, including narrow tunable emission with near unity quantum yields and very fast decay (Protesescu *et al* 2015). By embedding them in a suitable matrix such as organic polymers, one can obtain bright luminescent nanocomposite material with many applications, addressing at the same time their main drawback of poor environmental stability. Among many application fields, there is radiation detection with research ranging from low energy X-ray imaging to the high-energy physics (Chen *et al* 2018, Moulson 2022, Erroi *et al* 2023, Anand *et al* 2024). The promising timing capability in high-energy radiation detection of cesium lead bromide (CPB) NCs has been demonstrated on their thin films. They have been shown to be particularly promising for time-of-flight (TOF) techniques in positron emission tomography (PET) and computed tomography (CT) (Pagano *et al* 2024), where they have been utilized in combination with bulk scintillators in a heterostructure concept (Lecoq 2017), as well as for ultrasensitive real-time counting of single protons in proton therapy and radiotherapy (Mi *et al* 2024).

To produce nanocomposites with performance comparable to a layer of NCs, their stopping power needs to be comparably high translating into high NC loading in the matrix. For an estimate of required loading, we can use the work by Turtos *et al* (2019) who showed the fast timing potential of a NC layer of CdSe quantum dots and who also tested a 1 wt% CdSe nanocomposite. Based on their results and simulations, they estimated that loading more than 20 wt% might be needed in their case to achieve desired timing.

However, fabricating nanocomposites with a high content of luminescent NCs poses a serious challenge. In general, the agglomeration and aggregation of the NCs in the matrix introduces light scattering centers to the material, severely deteriorating its transparency, which hinders the ability to extract the light to the photodetector (Xu *et al* 2023). This issue becomes more pronounced as the loading of NCs in the matrix increases. Most of the work on CPB nanocomposites has been focused on the preparation of materials with low loading, typically around 1 wt% or lower (Cai *et al* 2022, Chhangani *et al* 2022, Pan *et al* 2022, Erroi *et al* 2023, Li *et al* 2023). However, the stopping power of such materials is insufficient for high energy radiation detection, e.g. a 1 mm thick nanocomposite of $CsPbBr_3$ in polystyrene with 1 wt% loading stops only 2% of 100 keV photons (see photon total attenuation cross sections in Supporting information). In a few works the authors have attempted to increase the loading of CPB nanocomposites to 10 wt% or higher (Maddalena *et al* 2021, Děcká *et al* 2022, Ghosh *et al* 2023). However, the transparency of the resulting materials quickly degraded with increased loading, proving the challenge of preparing high-quality, high-loading CPB nanocomposites while preserving a sufficient level of transparency to be extremely difficult.

To decrease the levels of NC agglomeration, grafting polymers to the NC surface is necessary as demonstrated in the preparation of nanocomposites of different materials. In particular, copolymerizable ligands have been very successfully deployed in the preparation of scintillating nanocomposites. For example, a transparent $La_xCe_{1-x}F_3$-polystyrene nanocomposite was achieved with 30 wt% loading (Sahi *et al* 2017). In another example (Liu *et al* 2017), a nanocomposite of $Cd_xZn_{1-x}S$/ZnS core shell quantum dots in polyvinyltoluene was prepared with a reported loading of up to 60 wt%, but the inorganic content, i.e. the actual concentration of pure NCs by themselves within the matrix was only 38.1 wt%.

The surface engineering of CPB NCs often faces challenges due to the ionic character of the material with its dynamic ligand bonding compared to traditional metal chalcogenide quantum dots (Swarnkar *et al* 2015, De Roo *et al* 2016). Nevertheless, several strategies of binding polymers to the CPB surface have already been investigated (Lee *et al* 2018, Kim *et al* 2019, Wu *et al* 2019, Imran *et al* 2021, Cai *et al* 2022, Pan *et al* 2022). However, none of these strategies have been used in attempts to prepare nanocomposites with a NC content exceeding 2 wt%.

In this work, we have prepared a polystyrene nanocomposite of cesium lead halide NCs with a loading of up to 40 wt%. The materials are translucent with partially preserved transparency which, to our best knowledge, has not been achieved thus far. To accomplish this, we employed novel surface engineering using allyltrimethoxysilane (ATMOS) and allyltrichlorosilane (ATS) to introduce a copolymerizable group to the NC surface. Our choice of ATMOS and ATS is based on an earlier report on alkyltrichlorosilanes employed for the synthesis of $CsPb(Br_{1-x}Cl_x)_3$, hereafter designated as CPBC NCs (Uddin *et al* 2018). In our work, when the alkyl functional group is replaced with that of allyl, we observe improvements in NC dispersion in the matrix and hence in the nanocomposite optical properties compared to the case with the common DDAB ligand used. By using ATS, the emission wavelength of the NCs can also be tuned at the same time by the anion exchange reaction of chloride anions released by hydrolysis. To assess the application potential of the prepared nanocomposites, their radioluminescence and timing properties were studied showing significant improvement of timing capabilities under X-ray excitation compared to previously reported values (Děcká *et al* 2022) proving their exciting potential for fast timing applications.

2. Experimental section

2.1. Chemicals

Acetone (p.a.,P-LAB), ATS (95%, Sigma-Aldrich), ATMOS (95%, Sigma-Aldrich), 2,2'-Azobis(2-methylpropionitrile) (98%, Sigma-Aldrich), didodecyldimethylammonium bromide (DDAB, 98%, Sigma-Aldrich), Cs_2CO_3 (99,9%, Sigma-Aldrich), ethyl acetate (p.a., PENTA), 1-octadecene (ODE, 90%, Sigma-Aldrich), oleic acid (OA, 90%, Sigma-Aldrich), oleylamine (OAm, 70%, Sigma-Aldrich), $PbBr_2$ (99 999%, Sigma-Aldrich), styrene ($\geq$99.5%, Carl Roth), and toluene (anhydrous, 99,8%, Sigma-Aldrich) were used. All chemicals were used as received without any further purification unless stated otherwise.

2.2. CPB synthesis and their surface functionalization

CPB NCs were prepared using a slightly modified original synthesis by Protesescu *et al* (2015). Cesium oleate was prepared using an increased 5:1 ratio of OA:Cs to be soluble at room temperature (Lu *et al* 2018). $PbBr_2$ was dissolved in octadecene using OA and oleylamine (OAm) and dried. Then pre-prepared cesium oleate

was injected at 170 °C and subsequently the reaction was quenched after 10 s in an ice bath. Following the synthesis, DDAB ligand exchange (Imran *et al* 2019) was performed and NCs were isolated and redispersed in toluene. Details about the synthesis can be found in Děcká *et al* (2021).

To prepare allyl-functionalized CPB NCs, 5 μl of ATMOS per 1 mg ml^{-1} of NC was added to the DDAB-CPB colloidal solution in toluene with a concentration of approximately 5 mg ml^{-1}. The colloidal solution was then stirred open to the ambient atmosphere for 24 h for hydrolysis to proceed. Afterward, the NCs were precipitated again by ethyl acetate and isolated by centrifugation for final redispersion to obtain the final solution for embedding in a polymer matrix. Toluene or styrene were used as dispersing environments.

To prepare allyl-functionalized CPBC NCs, the same procedure was followed, except that instead of using the ATMOS reagent, ATS was used to introduce the allyl functional groups. To obtain CPBC with various chloride content, a different amount of ATS was added: 1.4 μl of ATS per 1 mg of CPB for the CPBC1 sample, 2.8 μl of ATS per 1 mg of CPB for the CPBC2 sample and 5 μl of ATS per 1 mg of CPB for the CPBC3 sample.

2.3. Polymer nanocomposite preparation

First, to produce the nanocomposite sample, the styrene monomer was purified using an alumina column to remove the polymerization inhibitor. Then, a prepolymer was produced by heating the styrene to initiate its polymerization. The polymerization reaction was maintained at a steady rate for about 30 min to produce a viscous prepolymer. Subsequently, the prepolymer was mixed with the NC colloidal solution and 0.3 wt% of the initiator azobisisobutyronitrile. The polymerization was reinitiated by heating the mixture to 80 °C. The nanocomposite fully hardened in around 5 h.

To produce samples with high loading, it was not possible to obtain a concentration of the NCs in styrene high enough by directly redispersing the sediment after centrifugation. To increase the concentration of the NCs in styrene, a colloidal solution with the highest possible concentration was prepared and left undisturbed. When the vast majority of the NCs sedimented because the concentration was too high to be colloidally stable, most of the styrene above the sediment was carefully removed with a pipette. Then, a small amount of prepolymer was added and, after mixing it together, the nanocomposite was prepared as described above.

2.4. Characterization

Infrared spectrometry was performed on an FT-IR spectrometer (NICOLET iS50, Thermo Scientific) by the attenuated total reflectance technique on a diamond crystal. The spectrum was acquired in the mid-infrared region (400–4000 cm^{-1}; resolution: 2 cm^{-1}) and subsequently processed with SW OMNIC 9 (Thermo Scientific). High-resolution transmission electron microscopy imaging was performed on the FEI Titan Themis 60–300 cubed (TITAN) microscope at 300 kV. Transmission spectra and PL emission spectra were obtained using a FluoroMax spectrofluorometer (Horiba Jobin Yvon). Thermogravimetric and differential thermal analysis was carried out using a thermogravimeter (Labsys Evo, Setaram) with a crucible holder for 1200 °C and a corundum crucible. The temperature rate was 5 °C min^{-1} up to 500 °C, followed by cooling. RL spectra were obtained using a 5000 M spectrofluorometer (Horiba Jobin Yvon) with a monochromator, a TBX-04 (IBH Scotland) photodetector, and a Seifert X-ray tube (XRT) (40 kV, 15 mA) as an excitation source. The photoluminescence mapping measurements were realized on the Witec Raman Alpha300R equipment confocal microscope and spectroscope equipment. For the excitation two lasers with different wavelengths were used: UV laser (355 nm) for the excitation of CPBCs' Stokes PL and green laser (532 nm) for the excitation of CPBs' anti-Stokes PL. The optical power, objective magnification, and numerical aperture for the UV and green laser were 0.1 mW/5 mW, 100 × /40 ×, and 0.9/0.6, respectively. The integration time for a single point spectrum was 0.5 s with 10 integrations, in the case of PL mapping, the integration time was 0.03 s. The PL maps consist of 64 × 64 point spectra. The 3D PL maps consist of 30 stacks with their respective depth difference of 500 nm originating on the surface and ending in the depth of 15 μm.

The scintillation kinetics of CPB were measured in the time-correlated-single-photon-counting (TCSPC) mode (Bollinger and Thomas 1961) under X-ray excitation. Nanocomposite was irradiated with a pulsed XRT (N5084 from Hamamatsu) operating at 40 kV. The scintillation light was collected in reflection mode with a hybrid photomultiplier tube (HPM 100–07 from Becker&Hickl) optimized for TCSPC measurements. For a more detailed description of the experimental setup, please refer to Pagano *et al* (2022). The data were fitted with the convolution of the instrumental response function of the system (having 160 ps FWHM) and the intrinsic scintillation rate (Gundacker *et al* 2018, Pagano *et al* 2022). The latter was modeled as the sum of three exponential functions and the Dirac-delta function. This model was suggested by Děcká *et al* (2022) to properly take into account the ultra-fast emission of CPB NCs, on the trail of the one used by Gundacker *et al* (2018). to describe the scintillation time profile of BGO, which comprised both scintillation and prompt Cherenkov photons. The sample showed an instantaneous rise time that could not be resolved by the instrumental response function of the system. Since it was found that it did not improve the quality of the fit,

in order to have more stability on the decay part (as in the sum of exponential functions, the rise and decay components are correlated), the rise time was fixed at 0 ps.

The experimental setup and method used to measure the time resolution under X-ray excitation is thoroughly discussed by Pagano *et al* (2022). In brief, the samples were coupled to a SiPM (S13360-3050CS from Hamamatsu, 53 V breakdown voltage, 61 V bias voltage) collecting the scintillation light produced following X-ray excitation. The SiPM signal was read out by optimized high-frequency electronics, which separately process the time and energy information (Cates *et al* 2018, Gundacker *et al* 2019). As the authors used a pulsed XRT (N5084 from Hamamatsu), the time resolution was obtained as the FWHM of the time delay distribution between the SiPM signal and the external trigger of the XRT. By integrating the energy signal, information about the light output of the sample can also be obtained (Pagano *et al* 2022). For the measurements, $3 \times 3\,\mathrm{mm}^2$ plates were cut from the sample to match the active area of the SiPM. The optical coupling was done with the Meltmount glue (refractive index $n = 1.58$), and no reflective material was used to wrap the samples to avoid X-ray absorption from this material.

3. Results and discussion

3.1. Free NCs

CPB NCs prepared by hot-injection synthesis were highly crystalline, as seen in the HRTEM micrographs in figure 1(a), and exhibited an orthorombic crystal structure (see XRPD patterns in Supporting information). Upon addition of ATMOS to the NC colloidal solution, no structural or morphological changes were observed as confirmed by comparison with NCs with DDAB ligand, see HRTEM micrographs with determined interatomic distances in Supporting information. Furthermore, the formation of a thick SiO_2 shell was not observed, unlike in the case of tetramethoxysilane or tetraethoxysilane (Trinh and Ahmad 2024). This is probably due to steric hindrance of the organic groups and low concentration of reagents.

The extent of ligand changes following different steps in the synthesis, as described in the Experimental section above, was investigated using infrared spectroscopy (figure 1(b)). CPB OA NCs were a direct product of the hot injection synthesis and mostly only C–H vibrations were present in the spectra. After DDAB ligand exchange, a broad band centered around 3480 cm^{-1} and a band at 1588 cm^{-1} appeared in the spectra, which can be ascribed to N–H symmetric stretching and N–H bending, respectively. The successful introduction of DDAB is also evidenced by a broad band at 1080 cm^{-1}, characteristic of C–N^+ stretching vibrations (Zhang *et al* 2006). After ATMOS modification, the IR spectra exhibit the presence of siloxane polymers, evident by strong Si–O–Si vibrations at 1100 cm^{-1}, and allyl functional groups bound to Si, shown by characteristic bands at 1640, 1180, and 930 cm^{-1} (Launer and Arkles 2013). However, the vibrations of the N–H group of the DDAB ammonium group have not disappeared, pointing to only its partial replacement by allyl-modified siloxane polymers. Nevertheless, the introduction of the allyl copolymerizable groups, which was the objective of this surface modification, was successful.

Using ATMOS for the functionalization, the photoluminescence properties also remained unchanged compared to DDAB CPB NCs, as seen in figure 1(c), with only a small part of the spectrum at shorter wavelengths disappearing, which might be caused by one extra purification step after ATMOS modification. During centrifugation, the fraction of the smallest NCs (emitting in the blue part of the spectrum) remained in the discarded supernatant. Using ATS, the emission peak gets blue-shifted down to 440 nm and was tuned by various amounts of the reagent, which is shown in figures 1(d) and (e). This blue-shift is caused by anion exchange reaction introducing Cl^- anions from ATS molecules to the $CsPbBr_3$ lattice. Mixed bromochloride NCs produced were labeled CPBC1, CPBC2 and CPBC3 corresponding to increasing Cl^- content. The composition of produced CPBC NCs was estimated using X-ray fluorescence analysis to be $CsPbBr_{2.2}Cl_{0.8}$ for CPBC1 sample, $CsPbBr_{1.8}Cl_{1.2}$ for CPBC2, and $CsPbBr_{1.6}Cl_{1.4}$ for CPBC3. Details of analysis are provided in Supporting information.

3.2. Low-loading nanocomposites

NCs with DDAB ligand and allyl-functionalized NCs characterized in the previous subsection, were incorporated in the polystyrene matrix as described in Experimental section.

The effect of the partial replacement of DDAB by allyl-functionalized siloxane polymers on the aggregation and the final transparency of the material was studied on samples of CPB nanocomposites with the loading of 1 wt% and thickness of 750 μm. Two nanocomposites of DDAB-CPB NCs were prepared: one using NCs dispersed in toluene, which is the obvious choice since toluene is commonly used dispersant for such NCs and often used in nanocomposite preparation (Pan *et al* 2022, Ghosh *et al* 2023), and the other using NCs dispersed in styrene to reduce agglomeration effect promoted by toluene in the final sample, see the discussion below. Then, nanocomposite of allyl-functionalized NCs dispersed in styrene was fabricated.

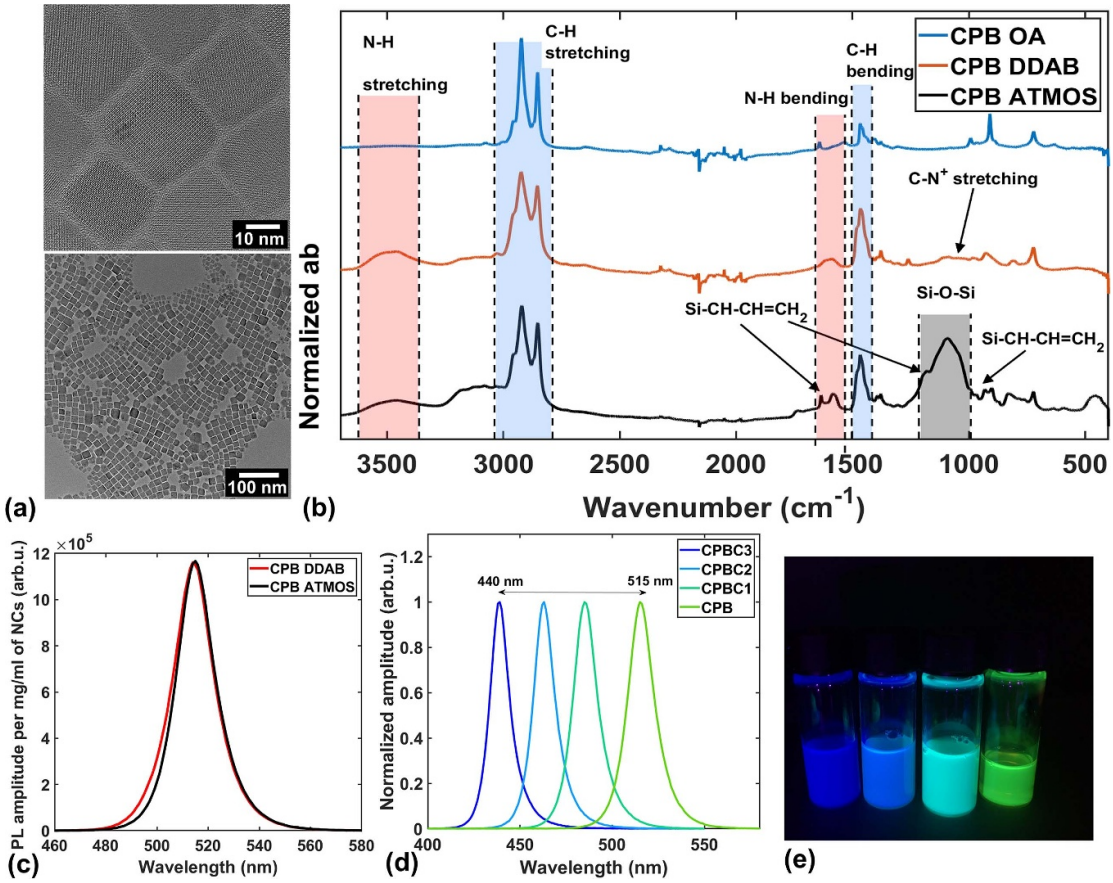

Figure 1. (a) HRTEM micrographs of CPB NCs after ATMOS functionalization. (b) Infrared spectra of CPB NCs with OA ligand isolated just after the hot-injection synthesis (blue), after DDAB ligand exchange reaction (red) and after ATMOS modification (black). (c) PL spectra of CPB NCs before ATMOS modification with DDAB ligand (black) and after ATMOS modification (red). (d) Normalized PL spectra of CPB and CPBC NCs with increasing chloride content. (e) Photo of respective CPB and CPBC samples in (d).

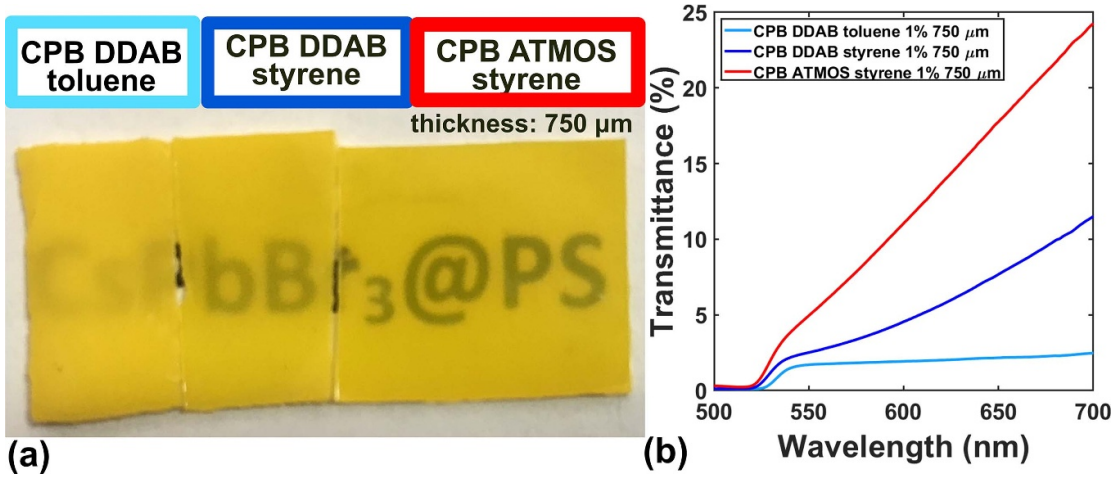

Figure 2. (a) Photo of CPB DDAB toluene, CPB DDAB styrene and CPB ATMOS styrene samples. (b) Transmittance spectra of CPB DDAB toluene sample (light blue), CPB DDAB styrene (dark blue) and CPB ATMOS styrene (red).

As seen in the photo of the samples in figure 2(a), the transparency in the sequence of samples (from left to right) gradually improves pointing to reduced levels of NC agglomeration. These apparent differences are quantified in the measured transmittance spectra in the figure 2(b) with twofold improvement of transmittance in the region of CPB emission.

First improvement in the transparency was caused by replacement of toluene as a dispersant by styrene. Being good solvent for many polymers and commonly used dispersant for CPB NCs, toluene is often used in

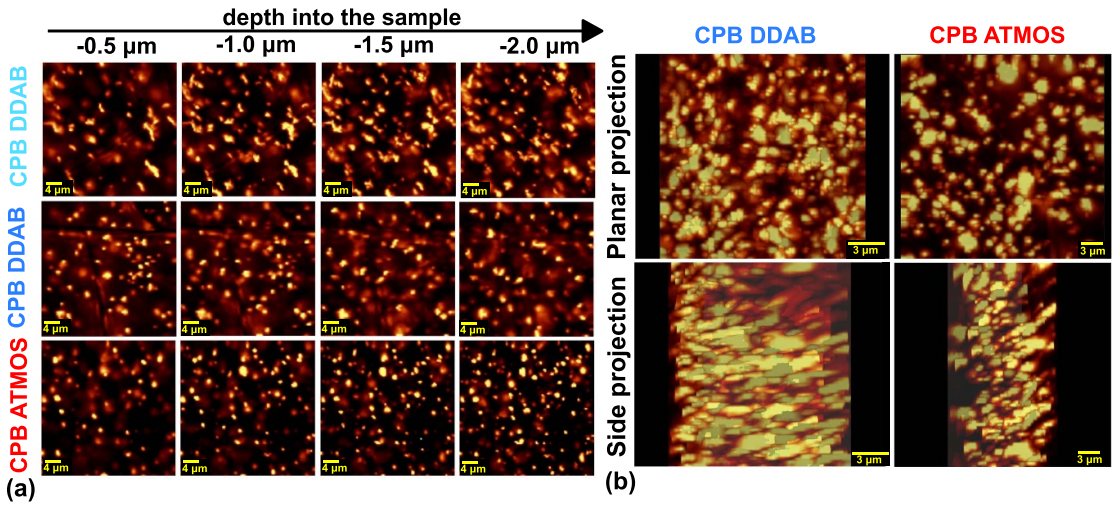

Figure 3. (a) PL integral intensity maps of the NC cluster distribution of CPB DDAB toluene, CPB DDAB styrene and CPB ATMOS styrene samples imaged at different depths of the nanocomposite. (b) Planar and side projections of 3D map of CPB DDAB styrene and CPB ATMOS styrene nanocomposites.

the literature during the preparation of CPB nanocomposites not only by solvent evaporation (Děcká *et al* 2022) but also by *in situ* polymerization (Pan *et al* 2022, Ghosh *et al* 2023). Here, however, toluene seems to promote the agglomeration of the NCs leading to deteriorated transparency. By eliminating it from the reaction by redispersing the NCs in the styrene monomer directly, initial improvement can be achieved. Another significant improvement in transparency was observed, when allyl-functionalized NCs are employed. The allyl group can copolymerize with the styrene (Lamparelli *et al* 2019), which is expected to form polystyrene chains covalently bound to the NC surface, reducing the phase segregation of the NCs in the matrix and thus leading to reduced NC agglomeration in the resulting nanocomposite.

To evaluate the levels of aggregation in different samples directly, confocal photoluminescence imaging (CPI) was used. Since CPB NCs exhibit bright anti-Stokes photoluminescence, the photoluminescence was excited by a green laser (532 nm), which is submitted to lower absorption than UV light. This allows us to collect the spatial distribution of the photoluminescence integral intensity not only from the surface but also from the volume of the nanocomposite to the depth of 15 μm, leading to the 3D imaging of the CPB NCs distribution. The spatial resolution of about 280 nm in the plane does not allow us to see the individual NCs, but the largest agglomerates and clusters of NCs in the matrix. Those are, however, crucial since they dominantly contribute to the light scattering and transparency reduction. In figure 3(a), the maps of integral luminescence intensity in various depths show the considerable difference in the cluster size and concentration of CPB DDAB samples and CPB ATMOS styrene sample confirming that the underlying change in NCs distribution influences significantly the transparency of the samples. The clusters in the allyl-functionalized sample are still present, meaning there is definitely room for further improvement; however, they are smaller than those in the conventional CPB DDAB samples. They also seem to be more uniformly distributed within the matrix, which can explain the increased transparency of this sample. For more detailed comparison of DDAB and ATMOS sample, nanocomposites of NCs dispersed in styrene were sequentially scanned to depth of 15 μm with the 500 nm step. Then the 3D map of the sample was constructed from obtained images with the intensity between different focal planes interpolated by a cubic spline (see supplementary data for animations). In figure 3(b), the projections of 3D maps are shown further highlighting the previous observations.

In figure 4, further details of the three samples from CPI is provided. The shape and peak position of the photoluminescence spectra averaged over the whole sampled area remain unchanged among the different samples. The presence of NC cluster in a depth of 12 μm is confirmed in PL integral intensity maps of the sample, while their size and distribution remain very similar to that in figure 3(a). Despite the clustering, the mean emission wavelength (MEW) is consistently around 530 nm in the whole sampled volume indicating that NC clustering results only in spatial agglomeration of NCs and not aggregation leading to formation of larger (nano)crystals. Despite the general homogeneity of MEW, some deviations in its value on the order of 1 nm can be observed. The position of clusters is associated with shorter MEW, while with increasing depth of sampling the MEW increases. This might be explained by slightly different levels of the sampled light reabsorption, where the emission from greater depths of the sample has to travel through more NC material shifting the MEW to longer wavelengths and vice versa.

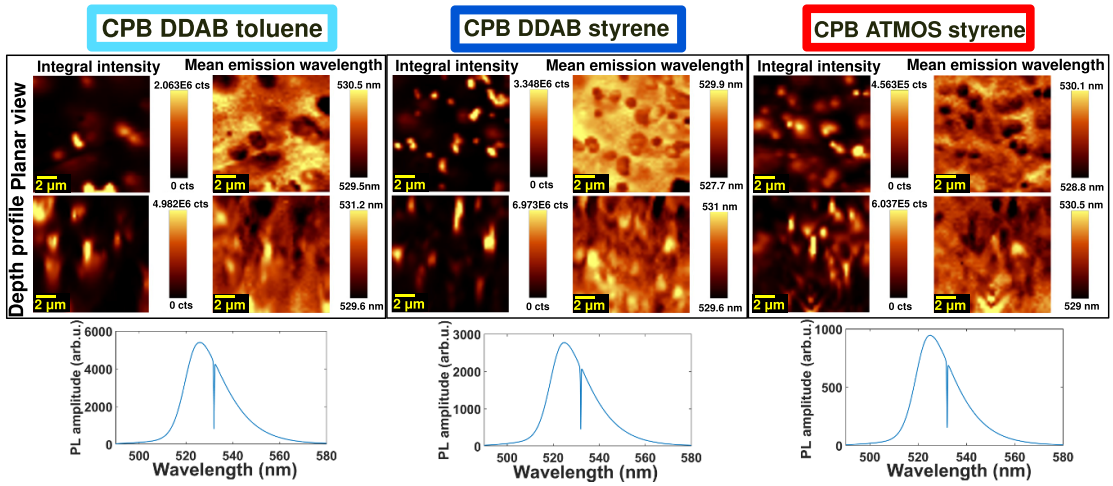

Figure 4. In the box: PL integral intensity and mean emission wavelength maps of CPB DDAB toluene, CPB DDAB styrene and CPB ATMOS styrene samples in both the planar view and depth profile. Below: PL emission spectra averaged over the whole sampled area of the respective samples.

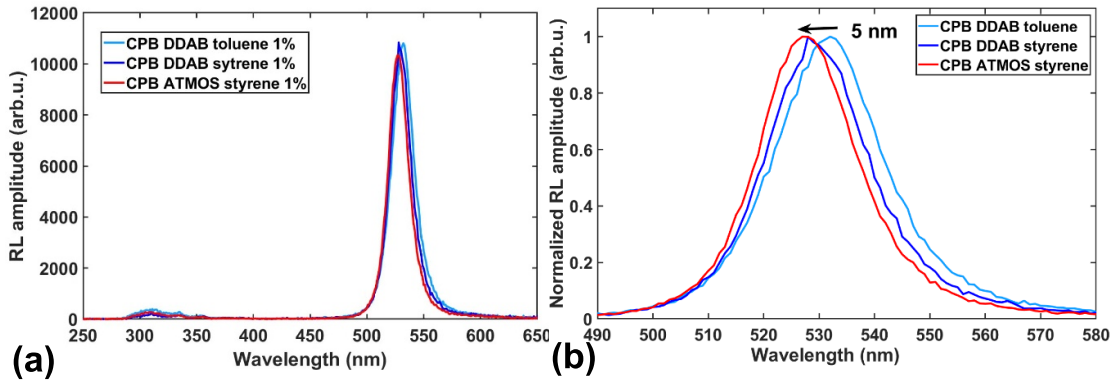

Figure 5. (a) RL spectra of CPB DDAB toluene (light blue), CPB DDAB styrene (dark blue) and CPB ATMOS styrene (red) samples. (b) Normalized RL spectra of the same samples as in (a) with marked blue-shift.

In radioluminiscence (RL) spectra (figure 5(a)), a narrow emission peak of CPB NCs is observed. In addition, there is also weak polystyrene emission centred around 320 nm (Gillispie 1993). Interestingly, the different transparency of the samples did not affect the overall RL intensity. However, a blue-shift of the emission maxima can be seen as the transparency of the samples improves (see figure 5(b)). This provides further evidence of different levels of agglomeration in samples. Formation of larger (nano)crystals and their clusters increases self-absorption and light scattering in the samples contributing to the shift. Our simulation using transmittance spectra estimates this effect to be approximately 1.3 nm (see Supporting information). The rest of the shift might be due to the shift of intrinsic NCs emission spectra due to increased mean NC size by agglomeration due to heating of the sample.

The nanocomposites of CPBC NCs resulting from the ATS surface modification were also produced and their properties compared at 1 wt% loading. In figure 6(a), photos of the prepared samples are shown demonstrating high visual transparency and in figure 6(b) samples of CPB and CPBC3 nanocomposites are shown under UV illumination. The transmittance of CPBC samples was generally higher than that of CPB which might be caused by different reactivity of ATS used for CPBC samples compared to ATMOS used for CPB sample resulting in better allyl-functionalization. For CPBC2 sample, a drop in transmittance at around 430 nm is observed caused probably by exciton absorption peak of NCs. The same effect, to lesser or no extent, can be also seen for CPBC1 and CPBC3 samples, respectively, indicating that in these samples, the overall NC concentration and/or sample thickness slightly varied and was lower, allowing a small fraction of the light to be transmitted, making the drop visible. In the RL spectra in figure 6(d), the trend of decreasing overall RL intensity with a chloride content was observed. This is consistent with literature where synthesised cesium lead chloride NCs have generally lower photoluminescence quantum yields (PLQY) which are caused

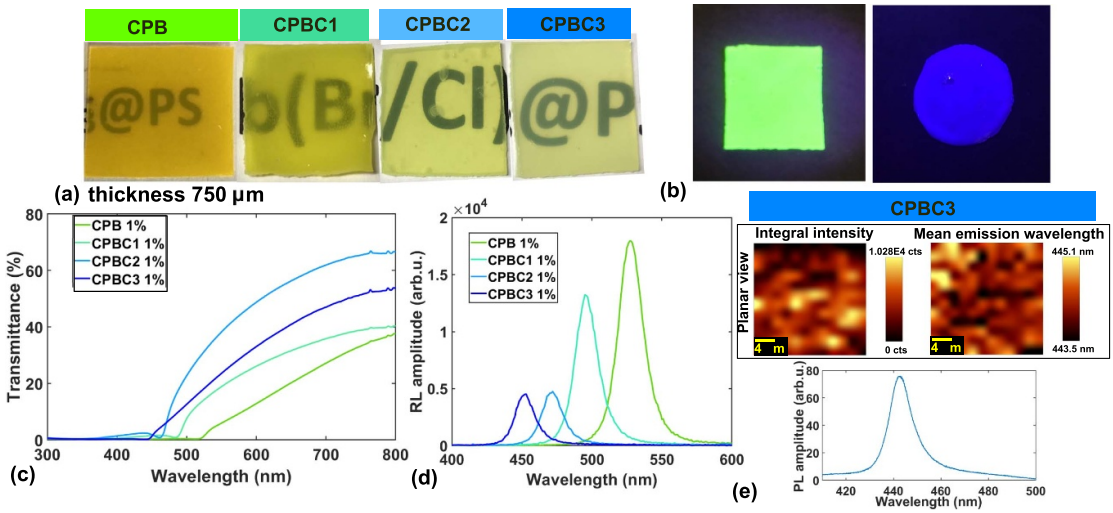

Figure 6. (a) Photos of CPB ATMOS (green), CPBC1 (blue-green), CPBC2 (light blue) and CPBC3 (dark blue) nanocomposites with 1 wt% loading. (b) CPB (on the left) and CPBC3 (on the right) nanocomposites under UV illumination. (c) Transmittance spectra of CPB and CPBC samples in (a). (d) RL spectra of CPB and CPBC samples in (a). (d) In the box: PL integral intensity and mean emission wavelength maps of CPBC3 1 wt% samples in planar view, below: PL emission spectra averaged over the whole sampled area of the respective sample.

by more significant nonradiative losses due to the presence of shallow and deep traps (Protesescu *et al* 2015, Erroi *et al* 2024).

Photoluminescence mapping of CPBC nanocomposites by CPI proved more challenging compared to the pure CPB samples. Due to different absorption properties of CPBC NCs, the 532 nm laser could not be used and the 355 nm laser was utilized instead. However, under intensive UV illumination (optical power $\geq$ 0.1 mW) rapid changes to photoluminescence spectra from narrow-band (blue) to broadband (white) peak were observed (see Supporting information). This might have been caused by the separation of chloride and bromide phases, similarly to the light induced phase separation observed for $MAPb(I_{1-x}Br_x)_3$ (Brennan *et al* 2017). For that reason, only mapping of CPBC3 nanocomposite is shown in figure 6(e). Nevertheless, PL integral intensity and MEW maps show even more homogeneous distribution of luminescence compared to CPB ATMOS sample with MEW around 444 nm, confirming better distribution of CPBC NCs in the matrix.

3.3. High-loading nanocomposites

The study of low-loading nanocomposites in the previous section showed great potential of allyl-functionalized NCs in the preparation of high quality, transparent nanocomposites. Due to the focus on application in radiation detection, our objective is to prepare high-loading nanocomposites with high stopping power.

Using the ATS ligand, CPBC nanocomposites with various chloride contents and 20 wt% loading of CPBC NCs were prepared, and 40 wt% loading was achieved for the CPB nanocomposite. Thanks to NC surface modification, some degree of transparency was preserved even at these levels of loading as can be seen in the photos in (figure 7(a)).

The total amount of inorganic content was studied by TGA, see figure 7(b). The subsequent EDX analysis of the inorganic residue (see SI) confirmed that the stoichiometric composition remained unchanged compared to the stoichiometry of CPB NCs powder, which was obtained by drying colloidal solution, and CPB NCs powder which was subjected to TGA heating program. Moreover, significant content of carbon was present only in dried CPB NCs powder sample without TGA heating procedure. Therefore, the determined NCs content in the nanocomposites is accurate and excludes the ligand shell, which is, unfortunately, not always of what reported in the literature, leading to frequent over-estimation of the NC content.

Taking this into account, to the best of our knowledge, 40 wt% of CLH NCs loaded in a plastic nanocomposite with such level of transparency has not yet been achieved in the literature. The highest reported NCs loading for CPB NCs is 50 wt% nanocomposite; this concentration was obtained by 'mixing QD powder and resin in different amounts' (Maddalena *et al* 2021), suggesting that the ligand shell is included in the NC weight. Moreover, the authors' objective was not to tackle the transparency issue, so the photo of only 40 wt% sample is presented, showing no transparency at all. Additionally, 50 wt% nanocomposite exhibits an afterglow pointing to severe aggregation of NCs in the sample and the presence of bulk phase characterised by the thermoluminescence glow peak around 100 K (Roda *et al* 2021).

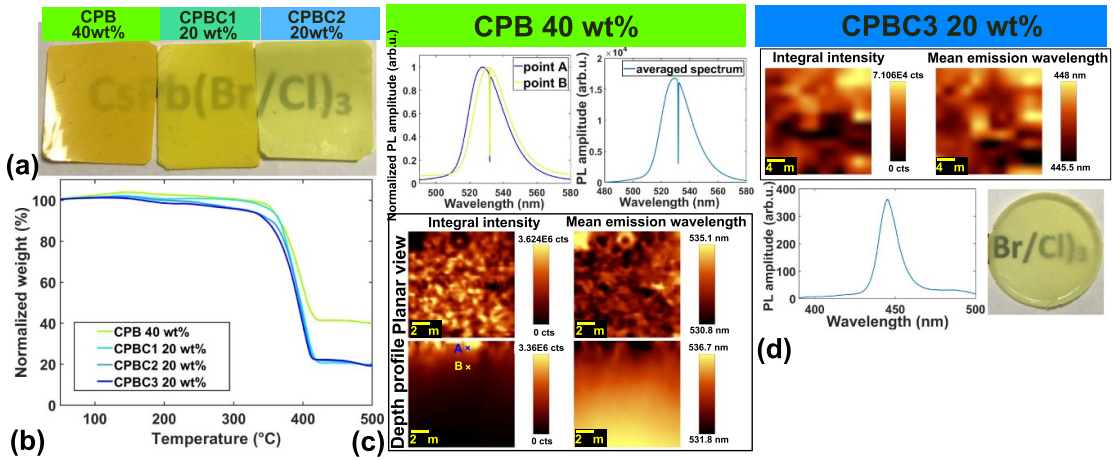

Figure 7. (a) Photo of CPB 40 wt% (green), CPBC1 20 wt% (blue-green) and CPBC2 20 wt% (light blue) nanocomposites. (b) Thermogravimetric curves of thermal decomposition of polystyrene matrix of CPB (green), CPBC1 (blue-green), CPBC2 (light blue) and CPBC3 (dark blue) nanocomposites. (c) Above: Normalized PL spectra at spots A and B in the CPB 40 wt% nanocomposite marked in PL integral intensity map and PL spectra of CPB 40 wt% nanocomposite averaged over the whole sampled area. Below: PL integral intensity and mean emission wavelength maps of CPB 40 wt% sample in both the planar view and depth profile. (d) In the box: PL integral intensity and mean emission wavelength maps of CPBC3 20 wt% sample in planar view. Below: PL emission spectra averaged over the whole sampled area and photo of the sample.

The overall highest reported NC loading with high transparency so far is 60 wt% of $Cd_xZn_{1-x}S/ZnS$ core–shell NCs in polyvinyltoluene, achieved by Liu *et al* (2017), using the same principle as here, i.e. co-polymerizable ligand shell. However, as above, this reported weight percentage also includes the ligand shell, and when subjected to the TGA, the determined inorganic content was only 38.1 w% (Liu *et al* 2017), meaning that, in fact, the authors achieved the same level of loading as we present here.

In PL integral intensity maps from CPI (see figure 7(c)), much more dense coverage of the sample with clusters is observed, however their distribution is quite homogeneous. Despite more clustering, given the higher NC concentration, the MEW of the PL in the position of the clusters remains the same (around 530 nm) as for samples with 1 wt% loading showing that preparation of nanocomposite with such high concentration did not lead to aggregation and formation of bigger particles or bulk phases. This is an evidence of efficient NC passivation by allyl-functionalization. In the depth profile we see quick decrease in amplitude of the signal when sampling from larger depths is attempted given mostly by limited penetration depth of the excitation light into the high loading sample. However, the PL intensity was also affected by reabsorption of the light which can be evidenced by very pronounced red-shift of MEW of the light sampled from larger depths, see comparison of PL spectra from points A and B whose position is marked in PL integral intensity map in depth profile in figure 7(c).

From CPBC samples, the mapping of the CPBC3 nanocomposite is presented in figure 7(d). Again, due to the PL changes under illumination, the resolution of the images is limited so the size of the clusters cannot be determined precisely, nevertheless the density of coverage increased and PL spectra integral intensity and position is relatively homogeneous.

In the RL spectra (figure 8(a)), the trend of decreasing RL intensity with an increasing chloride content can be observed as before, due to the lower PLQY of chloride perovskites. The RL intensity of 20 wt% CPBC1 nanocomposite was; however, comparable to that of 40 wt% CPB nanocomposite. With increasing loading to high levels, a rise in overall intensity was observed alongside with a more pronounced red-shift of the emission (figure 8(b)). Nevertheless, the rise of CPB 40 wt% intensity is not as high as one could expect, as evidenced by comparison with thick 1 wt% sample. Increasing the amount of NCs almost 4 times by increasing the thickness results in approximately 2 times higher intensity. However, increasing the amount of NCs 40 times by increasing the NC concentration in the matrix, the intensity rises only approx. 4 times. This result, along with the red-shift of the sample, points towards increased self-absorption which was observed in the CPI of the nanocomposite with 40 wt% where the shift of MEW up to 5 nm in a few μm of sample volume is seen.

The evidence of preserved optical properties of individual NC in the high loading nanocomposite from the CPI is complemented by comparable RL decay curves of CPB nanocomposites with 1 wt% and 40 wt% loading (see figures 9(a) and (b)). The CPB nanocomposites exhibit fast decay kinetics with ≈40%–45% of light emitted in the fastest components (the Dirac-delta function C_{amp} and the first exponential with the decay time of hundreds of ps). Then, the RL decay was significantly accelerated with increased chloride

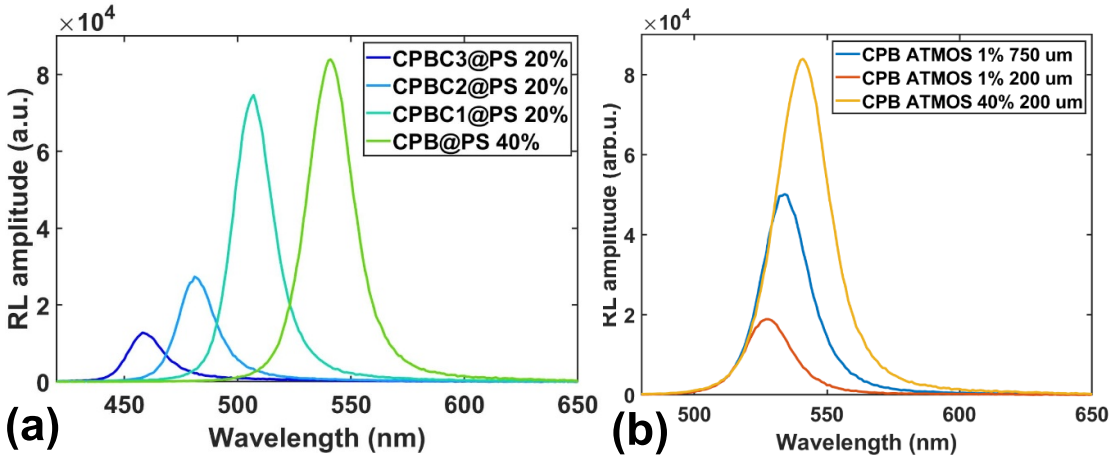

Figure 8. (a) RL spectra of nanocomposite samples of CPB (blue, CPBC1 (blue-green), CPBC2 (light blue) and CPBC3 (dark blue); (b) RL spectra of CPB ATMOS sample with 1 wt% loading and thickness of 200 μm (red) and 750 μm (blue) and CPB ATMOS sample with the 40 wt% loading and thickness of 200 μm (green);.

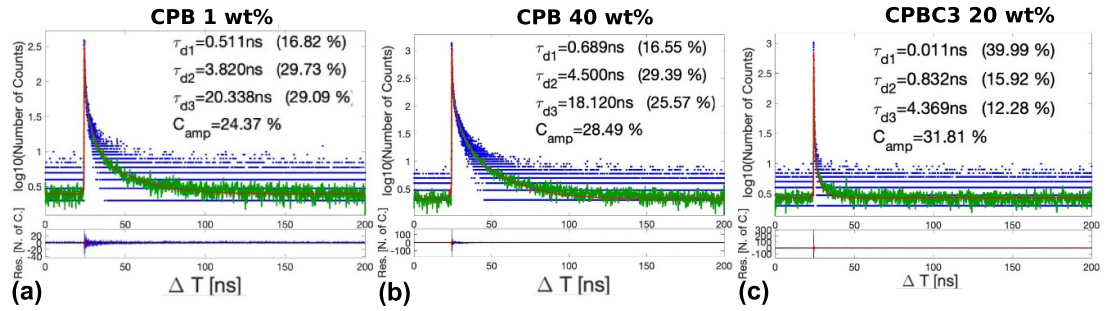

Figure 9. RL decay measurements of CPB ATMOS 1 wt%, CPB ATMOS 40 wt% and CPBC3 20 wt% samples. Experimental data are in blue, their average is in green and their three exponential fit with Dirac-delta function C_{amp} is in red, fit parameters are included for each sample.

content. This is expected and consistent with both the higher excitonic oscillator strength of chlorides (Diroll *et al* 2018) and lower PLQY of chlorides since their emission is more quenched by nonradiative losses leading to faster decays (Erroi *et al* 2024). For analysis, the CPBC3 sample with the highest chloride content was chosen and exhibited very fast decay time with the total of ≈70% of light emitted in the fastest components (figure 9(c)).

To evaluate the performance of samples as fast radiation detectors, the detector time resolution (DTR) was measured. In energy spectra (figure 10(a)), the light output of the samples can be compared looking at the endpoint of the distribution. The endpoint theoretically corresponds to the full energy deposition of 40 keV, however it is hard to estimate if the full energy deposition is possible in our sample. Nevertheless, the results are consistent with the RL spectra, CPB 40 wt% sample shows similar light output as CPBC1 20 wt% nanocomposite, while the sample with the highest chloride content exhibits much smaller light production.

However, the measured DTR of the high loading nanocomposites with different compositions (figure 10(b)) turned out to be comparable. This is probably caused by different decay kinetics of the samples as the time resolution is proportionate to initial photon density. The loss of light output in high chloride content samples might be fully compensated by acceleration of decay times due to increased presence of chlorides in the NC structure. Similar compensation effect between acceleration of effective decay times and decrease of scintillation yield by nonradiative losses through Auger recombination in CPB nanocomposites on coincidence time resolution was demonstrated by Erroi *et al* (2023).

Anyhow, the DTR value of about 175 ps is also a significant improvement compared to the previously reported value for the CPB nanocomposites of about 300 ps (Děcká *et al* 2022). Although, the values are not directly comparable since, in contrast to the work by Děcká *et al* (2022), the acquisition of the data was modified to trigger on events which record simultaneously the laser trigger signal, the timing, and the energy branch of the SiPM. For comparison, CPB nanocomposite with 40 wt% loading was measured with the old

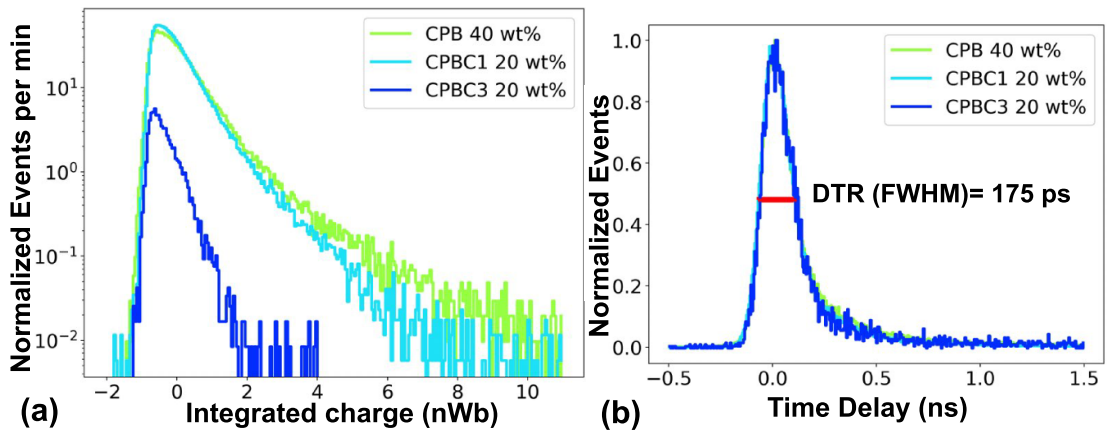

Figure 10. (a) Energy spectrum under X-ray irradiation of CPB 40 wt%, CPBC1 20 wt% and CPBC3 20 wt% for light output comparison; (b) time delay histograms of the same samples with inserted FWHM (equivalent to DTR) value.

settings and the value of 215 ps was recorded showing that the improvement in timing capabilities of CPB nanocomposites can be attributed mostly to enhancement of their properties.

Overall, the reported timing capabilities of our material combined with increase of loading to 40 wt% shows great promise for its applications in time-based radiation detector systems, e.g. for TOF-PET or TOF-CT. Such high levels of NC loadings provide significant improvement in stopping power for direct detection in TOF-CT systems (stopping now ≈ 25% of 100 keV photons). Meanwhile, in case of TOF-PET, 40 wt% NC content exceeds the requirements for nanocomposite loading in heterostructure concept estimated by Turtos *et al* (2019) and construction of such heterostructure will be focus of our next research. Regarding real-time single-proton demonstrated by Mi *et al* (2024), our nanocomposites might compare favorably to CPB thin films with tested thickness 50–120 μm thanks to superior transparency of our material leading to improved light extraction.

4. Conclusions

Allyl-functionalization using ATMOS and ATS proved successful in introducing allyl groups onto the $CsPbBr_3$ NC surface, leading to both improved NC dispersion in the polymer matrix and enhanced nanocomposite transparency. These functionalized NCs were utilized in preparation of high loading samples, achieving the NC content up to 40 wt%, which is so far the highest level of loading achieved while preserving certain level of transparency. Crucially, this approach offers simple and scalable surface modification in contrast to other polymer binding ligands which are often either not commercially available and require synthesis on their own, or they are too expensive as in the case of block-copolymers. Moreover, significant improvements in timing capabilities under X-ray excitation were achieved compared to previously reported values for CPB nanocomposites. This enhancement in timing capabilities, coupled with the increased stopping power, holds great promise for applications in TOF-PET or TOF-CT.

Data availability statement

The data that support the findings of this study are openly available at the following URL/DOI: https://doi.org/10.57680/asep.0601214.

Acknowledgments

This work was carried out in the frame of the crystal Clear collaboration and supported by the Czech Science Foundation, Grant Number GA23-05615S, the Ministry of Education Youth and Sports, Project 'Center for advanced applied science,' Grant Number CZ.02.1.01/0.0/0.0/16_019/0000778, OP JAC Project financed by ESIF and the MEYS SENDISO, Grant Number CZ.02.01.01/00/22_008/0004596, by the Grant Agency of the Czech Technical University in Prague, Grant Number SGS23/189/OHK4/3T/14 and received support from Pathfinder Open Project UNICORN (GA101098649). TEM characterization and photoluminescence mapping was performed at CEITEC Nano laboratories supported by MEYS CR under Project CzechNanoLab, Grant Number LM2023051.

ORCID iDs

Jan Král https://orcid.org/0000-0003-4694-7892
Kateřina Děcká https://orcid.org/0000-0002-2824-2381
Petr Liška https://orcid.org/0000-0003-0424-5366
František Hájek https://orcid.org/0000-0002-9344-4174
Michal Horák https://orcid.org/0000-0001-6503-8294
Václav Čuba https://orcid.org/0000-0002-6401-8117
Eva Mihóková https://orcid.org/0000-0002-6868-1426
Etiennette Auffray https://orcid.org/0000-0001-8540-1097

References

Anand A, Zaffalon M L, Erroi A, Cova F, Carulli F and Brovelli S 2024 Advances in perovskite nanocrystals and nanocomposites for scintillation applications *ACS Energy Lett.* **9** 1261–87
Bollinger L M and Thomas G E 1961 Measurement of the time dependence of scintillation intensity by a delayed-coincidence method *Rev. Sci. Instrum.* **32** 1044–50
Brennan M C, Draguta S, Kamat P V and Kuno M 2017 Light-induced anion phase segregation in mixed halide perovskites *ACS Energy Lett.* **3** 204–213,
Cai Y, Li W, Tian D, Shi S, Chen X, Gao P and Xie R-J 2022 Organic sulfonium-stabilized high-efficiency cesium or methylammonium lead bromide perovskite nanocrystals *Chem., Int. Ed.* **61** e202209880
Cai Y, Zhang P, Bai W, Lu L, Wang L, Chen X and Xie R-J 2022 Synthesizing bright $CsPbBr_3$ perovskite nanocrystals with high purification yields and their composites with in situ-polymerized styrene for light-emitting diode applications *ACS Sustain. Chem. Eng.* **10** 7385–93
Cates J W, Gundacker S, Auffray E, Lecoq P and Levin C S 2018 Improved single photon time resolution for analog SiPMs with front end readout that reduces influence of electronic noise *Phys. Med. Biol.* **63** 185022,
Chen Q *et al* 2018 All-inorganic perovskite nanocrystal scintillators *Nature* **561** 88–93
Chhangani S, Kumar M, Sahani R, Bera A and Pandya A 2022 Radiation polymerized CsPbBr3-PMMA nanocomposite for alpha particle detection *Mater. Today: Proc.* **48** 1028–31
De Roo J *et al* 2016 Highly dynamic ligand binding and light absorption coefficient of cesium lead bromide perovskite nanocrystals *ACS Nano* **10** 2071–81
Děcká K, Král J, Hájek F, Pruša P, Babin V, Mihóková E and Čuba V 2021 Scintillation response enhancement in nanocrystalline lead halide perovskite thin films on scintillating wafers *Nanomaterials* **12** 14
Děcká K, Pagano F, Frank I, Kratochwil N, Mihóková E, Auffray E and Čuba V 2022 Timing performance of lead halide perovskite nanoscintillators embedded in a polystyrene matrix *J. Mater. Chem.* **10** 12836–43
Diroll B T, Zhou H and Schaller R D 2018 Low-temperature absorption, photoluminescence and lifetime of $CsPbX_3$ (x = Cl, Br, I) nanocrystals *Adv. Funct. Mater.* **28** 1800945
Erroi A *et al* 2023 Ultrafast and radiation-hard lead halide perovskite nanocomposite scintillators *ACS Energy Lett.* **8** 3883–94
Erroi A *et al* 2024 Ultrafast nanocomposite scintillators based on Cd-enhanced CsPbCl3 nanocrystals in polymer matrix *ACS Energy Lett.* **9** 2333–42
Ghosh J *et al* 2023 Surfactant-dependent bulk scale mechanochemical synthesis of $CsPbBr_3$ nanocrystals for plastic scintillator-based X-ray imaging *ACS Appl. Nano Mater.* **6** 14980–90
Gillispie G D 1993 *Spectroscopic Characterization of Polymers: Fluorescence Principles* (American Chemical Society) pp 89–127
Gundacker S, Turtos R M, Auffray E, Paganoni M and Lecoq P 2019 High-frequency sipm readout advances measured coincidence time resolution limits in TOF-PET *Phys. Med. Biol.* **64** 055012
Gundacker S, Turtos R, Auffray E and Lecoq P 2018 Precise rise and decay time measurements of inorganic scintillators by means of X-ray and 511 KeV excitation *Nucl. Instrum. Methods Phys. Res.* A **891** 42–52
Imran M, Ijaz P, Goldoni L, Maggioni D, Petralanda U, Prato M, Almeida G, Infante I and Manna L 2019 Simultaneous cationic and anionic ligand exchange for colloidally stable $CsPbBr_3$ nanocrystals *ACS Energy Lett.* **4** 819–24
Imran M, Mai B T, Goldoni L, Cirignano M, Jalali H B, Stasio F D, Pellegrino T and Manna L 2021 Switchable anion exchange in polymer-encapsulated $APbX_3$ nanocrystals delivers stable all-perovskite white emitters *ACS Energy Lett.* **6** 2844–53
Kim H, So S, Ribbe A, Liu Y, Hu W, Duzhko V V, Hayward R C and Emrick T 2019 Functional polymers for growth and stabilization of $CsPbBr_3$ perovskite nanoparticles *Chem. Commun.* **55** 1833–6
Lamparelli D H, Speranza V, Camurati I, Buonerba A and Oliva L 2019 Synthesis and characterization of syndiotactic polystyrene-polyethylene block copolymer *Polymers* **11** 698
Launer P and Arkles B 2013 Silicon compounds: silanes and silicones *Infrared Analysis of Organosilicon Compounds* (Gelest Inc.)
Lecoq P 2017 Pushing the limits in time-of-flight pet imaging *IEEE Trans. Radiat. Plasma Med. Sci.* **1** 473–85
Lee S M, Jung H, Park W I, Lee Y, Koo E and Bang J 2018 Preparation of water-soluble $CsPbBr_3$ perovskite quantum dot nanocomposites via encapsulation into amphiphilic copolymers *ChemistrySelect* **3** 11320–5
Li Y, Xu Y, Yang Y, Jia Z, Tang H, Patel J B and Lin Q 2023 Template-assisted fabrication of flexible perovskite scintillators for x-ray detection and imaging *Adv. Opt. Mater.* **11** 2300169
Liu C, Li Z, Hajagos T J, Kishpaugh D, Chen D Y and Pei Q 2017 Transparent ultra-high-loading quantum dot/polymer nanocomposite monolith for gamma scintillation *ACS Nano* **11** 6422–30
Lu C *et al* 2018 Cesium oleate precursor preparation for lead halide perovskite nanocrystal synthesis: the influence of excess oleic acid on achieving solubility, conversion and reproducibility *Chem. Mater.* **31** 12
Maddalena F *et al* 2021 Stable and bright commercial CsPbBr3 quantum dot-resin layers for apparent X-ray imaging screen *ACS Appl. Mater. Interfaces* **13** 59450–9
Mi Z, Bian H, Yang C, Dou Y, Bettiol A A and Liu X 2024 Real-time single-proton counting with transmissive perovskite nanocrystal scintillators *Nat. Mater.* **23** 803–9
Moulson M 2022 The birth of nanocal (available at: ep-news.web.cern.ch/content/birth-nanocal)

Pagano F, Král J, Děcká K, Pizzichemi M, Mihóková E, Čuba V and Auffray E 2024 Nanocrystalline lead halide perovskites to boost time-of-flight performance of medical imaging detectors *Adv. Mater. Interfaces* **11** 2300659

Pagano F, Kratochwil N, Frank I, Gundacker S, Paganoni M, Pizzichemi M, Salomoni M and Auffray E 2022 A new method to characterize low stopping power and ultra-fast scintillators using pulsed X-rays *Front. Phys.* **10** 1021787

Pan A *et al* 2022 Luminescent and ultrastable perovskite-acrylate based elastomers with excellent stretchability and self-healing capability for flexible backlight display *Chem. Eng. J.* **433** 133590

Protesescu L, Yakunin S, Bodnarchuk M I, Krieg F, Caputo R, Hendon C H, Yang R X, Walsh A and Kovalenko M V 2015 Nanocrystals of cesium lead halide perovskites ($CsPbX_3$, X = Cl, Br and I): novel optoelectronic materials showing bright emission with wide color gamut *Nano Lett.* **15** 3692–6

Rodá C *et al* 2021 Understanding thermal and a-thermal trapping processes in lead halide perovskites towards effective radiation detection schemes *Adv. Funct. Mater.* **31** 2104879

Sahi S, Groza M, Zhang W, Do P, Kenarangui R, Burger A, Zhang J and Chen W 2017 High-loaded and transparent $La_xCe_{1-x}F_3$ - polystyrene nanocomposite scintillators for radiation detection *Can. J. Chem.* **95** 1233–40

Swarnkar A, Chulliyil R, Ravi V K, Irfanullah M, Chowdhury A and Nag A 2015 Colloidal CsPbBr3 perovskite nanocrystals: luminescence beyond traditional quantum dots *Angew. Chem., Int. Ed.* **54** 15424–8

Trinh C K and Ahmad Z 2024 SiO_2-coated lead halide perovskites core-shell and their applications: a mini-review *R. Soc. Open Sci.* **11** 3–6

Turtos R M *et al* 2019 On the use of CdSe scintillating nanoplatelets as time taggers for high-energy gamma detection *npj 2D Mater. Appl.* **3** 37

Uddin M A, Calabro R L, Kim D-Y and Graham K R 2018 Halide exchange and surface modification of metal halide perovskite nanocrystals with alkyltrichlorosilanes *Nanoscale* **10** 16919–27

Wu H *et al* 2019 Ultrastable inorganic perovskite nanocrystals coated with a thick long-chain polymer for efficient white light-emitting diodes *Chem. Mater.* **31** 1936–40

Xu X, Xie Y, Shi H, Wang Y, Zhu X, Li B, Liu S, Chen B and Zhao Q 2023 Light management of metal halide scintillators for high-resolution X-ray imaging *Adv. Mater.* **36** 2303738

Zhang L, Sun X, Song Y, Jiang X, Dong S and Wang E 2006 Didodecyldimethylammonium bromide lipid bilayer-protected gold nanoparticles: synthesis, characterization and self-assembly *Langmuir* **22** 2838–43